Journal of Magnetism and Magnetic Materials 454 (2018) 327–336

Contents lists available at ScienceDirect

Journal of Magnetism and Magnetic Materials

journal homepage: www.elsevier.com/locate/jmmm

Research articles

Kinetic Monte Carlo simulations of the effect of the exchange control layer thickness in CoPtCrB/CoPtCrSiO granular media

Ahmad M. Almudallal [a,*], J.I. Mercer [b], J.P. Whitehead [a], M.L. Plumer [a], J. van Ek [c]

[a] Department of Physics and Physical Oceanography, Memorial University of Newfoundland, St. John's, NL A1B 3X7, Canada
[b] Department of Computer Science, Memorial University of Newfoundland, St. John's, NL A1B 3X7, Canada
[c] 7206 Meadowdale Dr., Niwot, CO, 80503, USA

ARTICLE INFO

Article history:
Received 5 September 2017
Received in revised form 5 January 2018
Accepted 17 January 2018
Available online 2 February 2018

ABSTRACT

A hybrid Landau Lifshitz Gilbert/kinetic Monte Carlo algorithm is used to simulate experimental magnetic hysteresis loops for dual layer exchange coupled composite media. The calculation of the rate coefficients and difficulties arising from low energy barriers, a fundamental problem of the kinetic Monte Carlo method, are discussed and the methodology used to treat them in the present work is described. The results from simulations are compared with experimental vibrating sample magnetometer measurements on dual layer CoPtCrB/CoPtCrSiO media and a quantitative relationship between the thickness of the exchange control layer separating the layers and the effective exchange constant between the layers is obtained. Estimates of the energy barriers separating magnetically reversed states of the individual grains in zero applied field as well as the saturation field at sweep rates relevant to the bit write speeds in magnetic recording are also presented. The significance of this comparison between simulations and experiment and the estimates of the material parameters obtained from it are discussed in relation to optimizing the performance of magnetic storage media.

1. Introduction

The transition from in-plane to perpendicular media was one of several key technological advances that underpinned the exponential increase in the capacity of magnetic storage media over the last 20 years [1,2]. However, competing constraints imposed by grain size, thermal stability and switching field impose an upper limit on the areal bit density of single layer, perpendicular media. To alleviate these limitations, most current magnetic storage media is based on exchange control composite (ECC) materials in which the individual grains comprise several layers with adjacent layers separated by an exchange control (spacer) layer [3–6]. Varying the thickness of this layer in ECC media provides for a degree of optimization that allows for both a reduction in the switching field and an increase in the thermal stability.

Given the central role of ECC media in the continued development of magnetic storage media and the complex nature of its magnetic structure, modelling its properties is of importance. In this work, simulation results based on a micromagnetic model of interacting grains are compared with a series of experimental magnetization curves (MH hysteresis loops) obtained from vibrating sample magnetometer (VSM) measurements of dual layer ECC media. Both the methodology used in the simulations and the results obtained are of relevance to the optimization of ECC based storage media.

The modeling of magnetization curves of highly anisotropic materials at experimentally relevant temperatures and sweep rates based on standard micromagnetic models represents a significant challenge. Such materials typically show a strong sweep rate dependence as the grain reversal process is dominated by thermal activation involving large energy barriers ($\Delta E \gg k_B T$). As a consequence, the usual stochastic Landau-Lifshitz-Gilbert (sLLG) method [1,7], widely used in micromagnetics to simulate magnetic materials at finite temperature, is simply not feasible because of the long time scales involved. Perpendicular recording media used in hard disc drives represent an important class of such materials. By characterizing the relaxation process as a sequence of quasi-equilibrium states separated by thermally assisted grain reversals, kinetic Monte Carlo (kMC) provides an alternative approach to sLLG that can be applied to study such materials [8–16].

This work presents results based on a hybrid LLG/kMC formalism that has previously been applied to study single layer media [17] and MH loops of dual layer ECC media [18] at experimentally accessible sweep rates. As shown in earlier work, the parameters obtained from fitting experimental MH loops for ECC media based on LLG/kMC simulations at experimental sweep rates differ significantly from those obtained using sLLG that are limited to sweep

* Corresponding author.
E-mail address: ahmadam@mun.ca (A.M. Almudallal).

https://doi.org/10.1016/j.jmmm.2018.01.045
0304-8853/

rates several orders of magnitude greater than those used experimentally [19]. The simulation results presented here are compared with published experimental magnetization studies that examine the effect of the thickness of the exchange control layer in dual layer CoPtCrB/CoPtCrSiO ECC media [20].

Our results are based on a model of the ECC media grains that consists of two exchange-coupled Stoner-Wohlfarth particles and provide a quantitative estimate of the relationship between the thickness of the exchange control layer and the strength of the coupling between the layers. Other quantities of interest include the average energy barriers separating magnetically reversed states of the individual grains in zero applied field as well as the saturation field at high sweep rates. These are relevant to the long time decay of the signal to noise ratio of the stored data and switching fields at typical write speeds, respectively.

The outline of the paper is as follows. In Section 2, the hybrid LLG/kMC algorithm and its application to study dual layer ECC media is described. In Section 3, we present the methodology used in the determination of the parameters that characterize the magnetic properties of the individual ECC grains together with a detailed comparison of the simulation results based on the hybrid LLG/kMC algorithm and experimental MH loops for dual layer CoPtCrB/CoPtCrSiO ECC media [20]. A quantitative relationship between the thickness of the spacer layer and the strength of the interlayer coupling is obtained from these simulations. In Section 4, results for the average energy barriers separating magnetically reversed states of the individual grains in zero applied field as well as the saturation field at high sweep rates from the simulation results are presented. Their relevance to magnetic recording and storage media is discussed. In Section 5, the results are summarized together with possible future extensions of the methodology and its application to ECC media.

2. The model and the hybrid LLG/kMC algorithm

The simulations are based on a model in which each of the grains is represented by two exchange-coupled Stoner-Wohlfarth particles, which we label as a (cap layer) and b (granular oxide layer). The volumes of the a and b layers comprising the grains, and the cross sectional area of the interface separating them, are denoted by v_a, v_b and A, respectively. The energy of the kth grain may then be written as

$$\begin{aligned} E_k = &- K_a^k v_a (\hat{m}_a^k \cdot \hat{n}_a^k)^2 - K_b^k v_b (\hat{m}_b^k \cdot \hat{n}_b^k)^2 - IA\,(\hat{m}_a^k \cdot \hat{m}_b^k) \\ &- \vec{M}_a^k \cdot \bar{\Gamma}_{aa}^k \cdot \vec{M}_a^k - \vec{M}_b^k \cdot \bar{\Gamma}_{bb}^k \cdot \vec{M}_b^k - \vec{M}_a^k \cdot \bar{\Gamma}_{ab}^k \cdot \vec{M}_b^k \\ &- \sum_{k \neq k'} \left(\vec{H}_{kk'}^a \cdot \vec{m}_a^k + \vec{H}_{kk'}^b \cdot \vec{m}_b^k \right) - \vec{H} \cdot (\vec{m}_a^k + \vec{m}_b^k) \end{aligned} \tag{1}$$

where $\vec{H} = H\hat{z}$ is the perpendicular applied magnetic field, $K_l^k, \hat{n}_l^k$ and $\vec{M}_l^k$ are the anisotropy constant, anisotropy axis and the magnetization vector in each of the layers ($l \in \{a, b\}$), respectively, with $\vec{m}_l^k = \vec{M}_l^k v_l$ and $\hat{m}_l^k = \vec{M}_l^k / M_l^k$. $\bar{\Gamma}_{ab}^k$ denotes the magnetostatic tensor between the layers a and b, with $\bar{\Gamma}_{aa}^k$ and $\bar{\Gamma}_{bb}^k$ denoting the magnetostatic shape anisotropy for the layers a and b. $\vec{H}_{kk'}^l$ is the interaction field (exchange stiffness A_l plus magnetostatic) acting on the lth layer ($l \in \{a, b\}$) of the kth grain due to the k'th grain, and IA represents the exchange interaction between the a and b layers within a single grain.

The simulation of the MH loops using the hybrid LLG/kMC approach is described in some detail for both single and dual layer materials in Refs. [17,18]. The simulation begins with the system in a fully saturated state with an applied field H_0. The saturated state is then input into an LLG ($T = 0$) simulation and relaxed to a local minimum energy state, which we denote by $\mathcal{S}_0$, and the interaction field $\sum_{k' \neq k} \vec{H}_{k'k}^l$ calculated for each layer ($l \in \{a, b\}$) in each grain ($1 \leqslant k \leqslant L \times L$). The energy of each grain may then be calculated as a function of $\hat{m}_l^k$ and the local minimum energy states for each grain is determined. For grains with more than a single local minimum energy state we compute the rate constants $r_{i \to j}^k$ between each pair of local minimum energy states based on the Arrhenius-Néel expression

$$r_{i \to j}^k = f_{ij}^k \exp\left(-\frac{\Delta E_{ij}^k}{k_B T} \right) \tag{2}$$

where the ordered pairs $\{ij\}$ label the local minimum energy states in the kth grain connected by a minimum energy path (MEP). ΔE_{ij}^k and f_{ij}^k denote the energy barrier and attempt frequency separating the initial local minimum energy state i from the final state j. From the rate constant, the set of wait times $t_{i \to j}^k = (r_{i \to j}^k)^{-1} \log x$, where x is a uniformly distributed random number between 0 and 1, is calculated for each of the grains and the grain with the minimum wait time $t_R = \min[t_{i \to f}^k]$ determined. Denoting the index of this grain as k_R, the quantity t_R is referred to as the time to first reversal and essentially determines the time at which the grain k_R undergoes a reversal from some initial state i to some final state f. If t_R is less than some user specified time interval Δt then a new state $\mathcal{S}_1$ at time $t_1 = t_R$ is constructed in which the grain at $k = k_R$, initially in state i, is replaced with the grain in state f and the system is allowed to relax to some new local equilibrium with $H = H_1 = H_0 - R t_R$, where $R = |dH/dt|$ denotes the sweep rate. If, on the other hand, $t_R \geqslant \Delta t$, then the kth grain remains in the state i and $\mathcal{S}_1 = \mathcal{S}_0$ and the system is allowed to relax to some new local equilibrium with $H = H_1 = H_0 - R\Delta t$. This process is repeated generating a sequence of states $\{\mathcal{S}_0, \mathcal{S}_1 \ldots\}$ at times $\{t_0, t_1 \ldots\}$ until the normalized magnetization $M(\mathcal{S}_n) < -M_s$, where $M_s < 1$ is some nominal value used to define saturation.

The application of kMC to the case of single layer media is relatively straightforward [17]. Each grain typically has a maximum of two local energy minima and the location of these local minima, the saddle points connecting them can be performed analytically [21] and the associated rate constants evaluated [18]. The dual layer case on the other hand presents a number of challenges. The most obvious is the fact that it requires the numerical determination of the local energy minima, the saddle points connecting them and the associated rate constants for each grain at each kMC step. This is a formidable task and the efficiency and stability of the algorithm used largely determines the feasibility of the kMC method.

In the present work, we discretize the unit sphere that describes the state-space of a single spin by triangulating the surfaces of dodecahedron inscribed by the unit sphere and projecting the vertices onto the surface of the sphere resulting in a 3-polytope polyhedron. The discretization process is described in some detail in Appendix A. The location of the local minimum energy states of the ECC grains are obtained by taking the vertices of the polyhedron as initial states and relaxing them to a local energy minimum using a steepest descent algorithm. States that coincide with a certain tolerance are then merged to give the local minimum energy states of the grain. All the paths between any two local minimum energy states can then be constructed from the edges of the polyhedron and the minimum energy path on the lattice determined using a modified Bellman-Ford algorithm [22]. This provides an initial estimate of the location of the saddle points that can be further refined by repeatedly fitting the energy surface to a quartic and solving for the saddle point algebraically. From this the energy barrier separating the two states and the attempt frequency may be calculated [18].

In addition to the complexity of the energy landscape of dual layer ECC grains, the variation in the energy barriers can give rise to a range of rate constants that span several orders of magnitude. Transitions between states separated by low energy barriers do not contribute significantly to the MH loops at experimental sweep rates as the rapid fluctuations between these transient states mean that they quickly equilibrate. However, such fluctuations can significantly impact the efficiency of the kMC algorithm. How to best to treat such fluctuations is an outstanding problem that can restrict the applicability of the kMC algorithm [23].

The LLG/kMC code used here is programmed to detect the onset of high frequency fluctuations by identifying grains that return to their initial state after N kMC steps (in the present code N is set to 32). When these high frequency fluctuations are detected, local minimum energy states that are connected by an energy barrier less than some predetermined threshold are combined into clusters. The kMC is then reformulated in terms of a combination of local minimum energy states and clusters [18]. If the fluctuations persist, then the threshold is increased by a factor of 2 until such time as the high frequency fluctuations are suppressed and the time between successive kMC steps is appropriate. The threshold is then gradually reduced until the high frequency fluctuations reappear. As shown in Ref. [18], this can lead to significant increases in performance with little loss in accuracy.

3. Simulation of dual layer ECC media

In the present model, grains are arranged on a $L \times L$ square lattice with periodic boundary conditions (where $L = 32$). The anisotropy constant, anisotropy axis and the magnetization are assigned grain-to-grain Gaussian distributions of values. The granular oxide and cap layers were 14 nm and 4 nm thick, respectively, as used in the experimental study [20]. Lateral grain dimensions were 7 nm × 7 nm. The finite thickness of the exchange control layer, d, was not included in the grain geometry. A sweep rate of $R = 7.5$ kOe/s at temperature $T = 300\ K$ was used in both the simulation and experimental studies. The material parameters used in the simulations to fit the experimental data are shown in Table 1 and were determined as follows. Assumed values for the intralayer exchange stiffness parameter, denoted as A_a and A_b, were guided by previous modelling results on generic ECC media for the cap and granular oxide layers, with moderate and weak coupling, respectively [19]. Experimental values for M_a, M_b, K_a and K_b (see Table 1) served as a starting point for these parameters in the MH loop fitting procedure. To simplify fitting the MH loops for the dual layer media, we first fit the kMC MH loop to the experimental results for only the granular oxide layer. Best results were achieved using the magnetization and anisotropy values indicated in Table 1, along with a 10% variance in K_b and M_b among the grains, as well as a 4° variance in anisotropy axis direction about z. For this purpose a standard Gaussian distribution was used.

Table 1
Parameters used in modelling the cap layer (M_a, K_a and A_a) and the granular oxide layer (M_b, K_b and A_b). Experimental values were extracted from Ref. [20].

Cap Layer	M_a	K_a	A_a
Experimental	425	2.20×10^6	–
Simulation	450	2.10×10^6	2.0×10^{-6}
Granular Oxide Layer	M_b	K_b	A_b
Experimental	385	3.10×10^6	–
Simulation	385	3.05×10^6	0.018×10^{-6}
Units	(emu/cc)	(erg/cc)	(erg/cm)

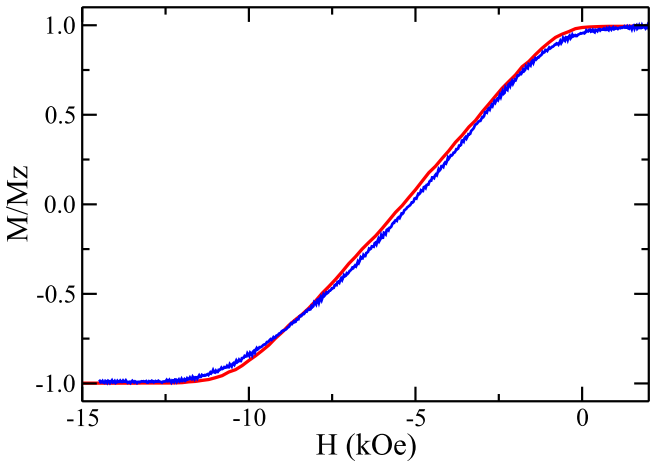

Fig. 1. Normalized magnetization as a function of applied field for the 14 nm granular oxide layer, CoPtCrSiO, at a sweep rate $R = 7.5$ kOe/s from experimental data (blue) and kMC simulations (red). (For interpretation of the references to colour in this figure legend, the reader is referred to the web version of this article.)

The outcome of this procedure is shown in Fig. 1 and illustrates excellent agreement between simulation and experimental results.

Having established model parameters for the granular oxide layer, the hybrid LLG/kMC algorithm was then applied to best reproduce the experimental MH loops in the dual layer case [20]. Here, the values of the magnetization, anisotropy and exchange stiffness of the cap layer, together with the interlayer exchange constant I were estimated by fitting the MH loops obtained from the simulation results with the corresponding experimental data with a spacer thickness of $d = 3.0$ nm. For this layer, a larger 20% variance in K_a and M_a (along with the same 4° variance in anisotropy axis) were found to provide a good description of the experimental data. Values of M_a, K_a and A_a are presented in Table 1, while a value of $I = 0.05\,\mathrm{erg/cm^2}$ was used for the interlayer exchange coupling constant. The MH data obtained from the simulations together with the experimental data for $d = 3.0$ nm are plotted in Fig. 2 (top left).

Assuming that, to leading order, the magnetic parameters for the granular oxide and cap layers given in Table 1 are not affected by the thickness of the spacer, only the value of the exchange parameter I was adjusted to achieve the best overall agreement between the simulations and the experimental data for $d < 3.0$ nm. The parameter fitting was done by eye based on a single kMC run for each value of d. Once a reasonable fit had been obtained a series of 10 LLG/kMC runs were performed for each parameter set and averaged to produce the results presented in Fig. 2. In Fig. 3, the resulting values of the exchange parameter I plotted against the exchange control layer thickness d and show a roughly linear decrease of I as a function of increasing d. To our knowledge this is the first calculation that establishes a quantitative relationship between the experimental exchange control layer thickness and the strength of the interlayer exchange in ECC media based on experimental MH loops.

The MH loops obtained from the simulations shown in Fig. 2 give good quantitative agreement with the experimental data, and successfully capture their essential features. Fig. 4 presents a comparison of the nucleation, coercive, and saturation fields H_n, H_c, and H_s, respectively, estimated from experimental and simulation results, with the definitions $M(H_n) = 0.95$, $M(H_c) = 0.0$ and $M(H_s) = -0.95$, respectively. The nucleation and coercive fields show good agreement between the simulation and experiment but is less satisfactory for the saturation field. In particular, the experimental values exhibit a well defined minima in H_s for

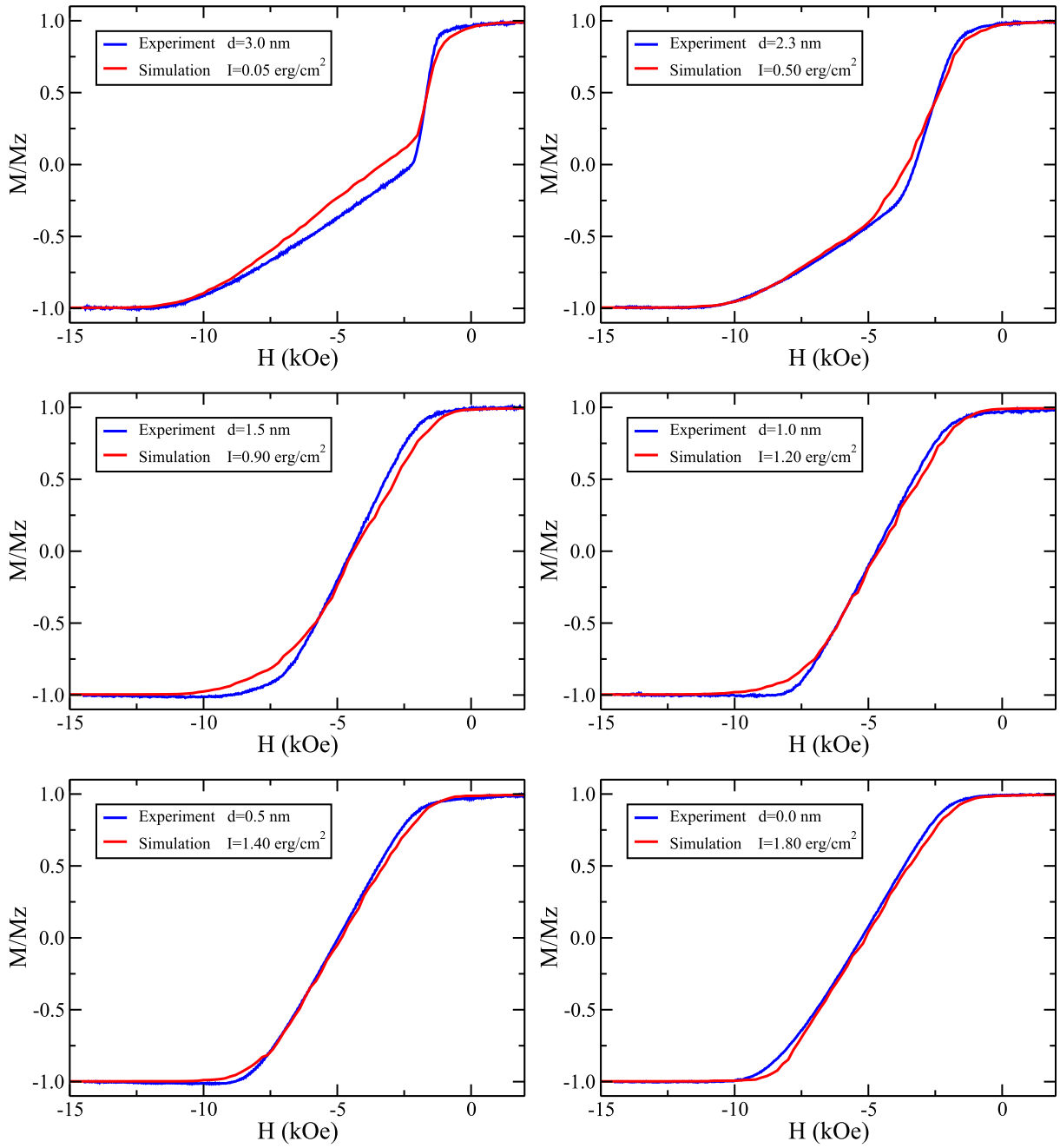

Fig. 2. MH loops for dual layer ECC CoPtCrB/CoPtCrSiO media for a sweep rate of $R = 7.5$ kOe/s calculated from experimental data (blue) for several values of d together with the corresponding fit from kMC simulations (red). (For interpretation of the references to colour in this figure legend, the reader is referred to the web version of this article.)

$d \approx 1.0$ nm, a feature that is absent in the simulation results. Examining the MH loops presented in Fig. 2 the discrepancy between the experimental values of H_s and those determined from the simulations is due in part to the shape of the tail of the MH curve in the region $H \approx H_s$. Fig. 2 also shows that the simulation results underestimate the drop in the magnetization observed at $H \approx 2$ kOe for $d = 0.05$ nm case.

4. Energy barriers and switching fields

In the previous section it was demonstrated how a detailed comparison of the experimental MH loops and simulation studies provided a quantitive relationship between the interlayer exchange coupling constant (I) between the layers and the spacer thickness (d). The model parameters obtained from this comparison also allow other quantities of direct relevance to magnetic recording and storage to be evaluated. An important example is the reduction in the signal to noise ratio of the bit pattern stored on magnetic media over time due to thermally activated grain reversal in zero applied field. The rate of thermally activated grain reversal will be proportional to the Arrhenuis-Néel factor $(\exp(-\Delta E/k_B T))$ where ΔE denotes the energy barrier separating spin reversed states of the individual grains in zero field. Using the parameters given in Table 1 with the variances cited in Section 3, the distribution of energy barriers in zero applied field has been calculated for both the single granular oxide layer and for a system of ECC coupled grains for several values of I over the range $0.05\ \text{erg/cm}^2 \leqslant I \leqslant 3.0\ \text{erg/cm}^2$ (note this extends the range

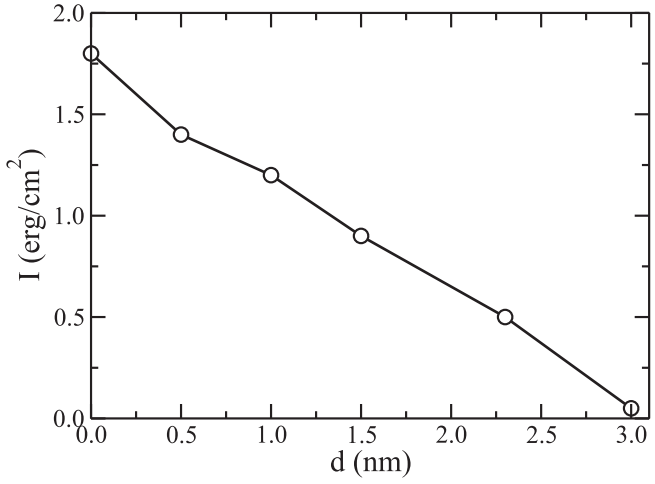

Fig. 3. Relationship between the interlayer coupling constant I and the exchange control layer thickness d obtained from fitting the simulation results with experiment shown in Fig. 2.

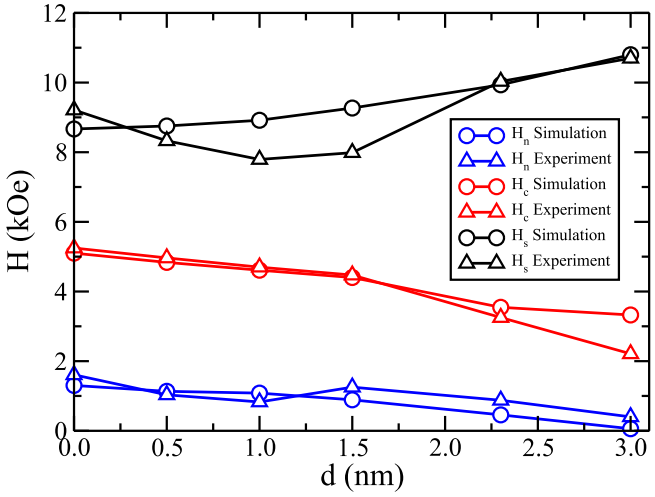

Fig. 4. Nucleation, coercive, and saturation fields H_n, H_c and H_s as a function of d for both experimental and kMC simulation. The value of d for the kMC simulations is inferred from Fig. 2

of I values from a maximum of $I = 1.8\,\mathrm{erg/cm^2}$ used in the previous section to fit the data to $I = 3.0\,\mathrm{erg/cm^2}$). In Fig. 5 we show a plot of $\Delta E(\mathrm{ECC})/\Delta E(\mathrm{SL})$, the ratio of the average energy barriers separating the spin reversed magnetic states in the individual dual layer grains in zero applied field, normalized with respect to the corresponding average calculated for the single layer case, as a function of the interlayer coupling constant I. We note that for the case of very weak coupling $I = 0.05\,\mathrm{erg/cm^2}$ this ratio is very close to unity, as we would expect, and increases with increasing I. This increase illustrates the stabilizing effect of the exchange coupled cap layer on the decay of the signal to noise ratio due to thermal activated grain reversal. We also note that this ratio does not appear to have reached its saturation value corresponding to a completely coherent rotation of the grains [18].

In the case of single layer media with perpendicular anisotropy, this increase in the thermal stability of the bit pattern is typically achieved by increasing either the bit size, which reduces the areal bit density, or increasing the anisotropy constant, which increases the switching field required to write to the media. The advantage of ECC media is that the effect of the exchange coupled cap layer

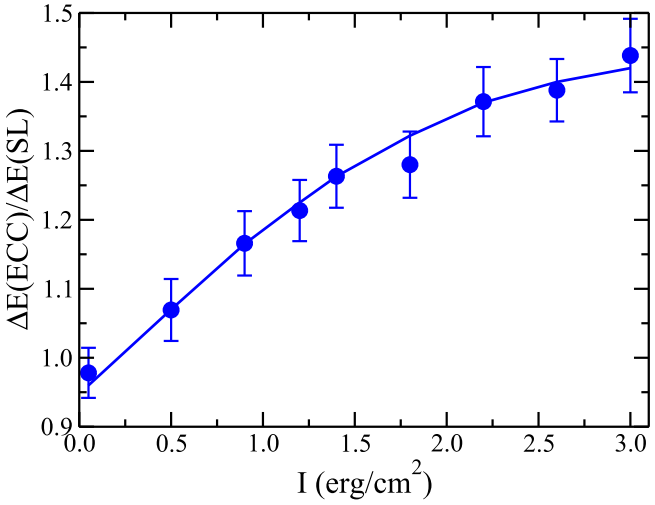

Fig. 5. Average energy barrier, $\Delta E(\mathrm{ECC})$, calculated for the dual layer system normalized by the corresponding value for the single layer, $\Delta E(\mathrm{SL})$, for a system allowed to relax to equilibrium from the fully saturated state for $H = 0$.

not only increases ΔE, as shown in Fig. 5, it also reduces the saturation field as shown in Fig. 4. As discussed in the introduction, it is the combination of increased thermal stability combined with lower switching fields that is the reason why virtually all current magnetic storage media are fabricated from ECC based materials.

Another important quantity that can also be calculated from the parameters obtained from fitting these VSM based loops is the saturation field at sweep rates relevant to the write process in magnetic media. As discussed in the introduction these rates are typically several orders of magnitude higher ($R \sim 10^7$ kOe/s) than those used in VSM measurements. The rate dependence of H_s can be clearly seen in the simulation results shown in Fig. 6, in which MH loops are presented for the single granular oxide layer for both $R = 7.5$ kOe/s and $R = 10^7$ kOe/s. The simulation data for the higher sweep rate $R = 10^7$ kOe/s was calculated using the finite temperature sLLG with a value of $\alpha = 0.1$. The latter ($R = 10^7$ kOe/s) show a significantly higher saturation field, $H_s(\mathrm{SL}) = 15.6$ kOe, than the value $H_s(\mathrm{SL}) = 10.7$ kOe obtained using VSM sweep rates ($R = 7.5$ kOe/s).

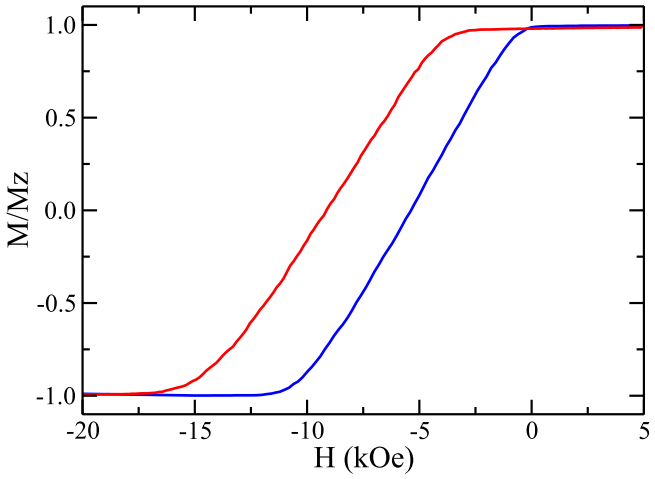

Fig. 6. Normalized magnetization as a function of applied field for the 14 nm granular oxide layer, CoPtCrSiO, at a sweep rate $R = 7.5$ kOe/s from kMC simulations (blue) and $R = 10^7$ kOe/s from sLLG simulations (red). (For interpretation of the references to colour in this figure legend, the reader is referred to the web version of this article.)

In order to examine the effect of the cap layer on the saturation field at these higher sweep rates, the kMC simulations presented in Section 3 for dual layer ECC grains at $R = 7.5$ kOe/s have been extended to cover a wider range of interlayer coupling $0 \leqslant I \leqslant 3.0$ erg/cm^2 and compared with loops calculated from a series of sLLG simulations [24] on dual layer ECC grains for $R = 10^7$ kOe/s again with $\alpha = 0.1$. As in the single layer case the values of the saturation field obtained for the ECC grains (H_s(ECC)) at the higher sweep rate are significantly larger than those obtained using the VSM sweep rates. To demonstrate how the effectiveness of the cap layer at the higher sweep rates, results for normalized saturation fields H_s(ECC)/H_s(SL) are plotted in Fig. 7 as a function of interlayer exchange constant I for both $R = 7.5$ kOe/s and 10^7 kOe/s. It should be noted that while the curves shown for $R = 10^7$ kOe/s in Figs. 6 and 7 were calculated using sLLG, in Appendix B it is shown that similar results can be obtained at those sweep rates using the hybrid LLG/kMC. This is consistent with earlier studies [17] and demonstrates that the differences between the simulation data shown in Figs. 6 and 7 are due to the sweep rate dependence rather than the particular method used to calculate the field dependence of the magnetization. As discussed below the results presented in Fig. 7 show a number of interesting features.

The first point to note in Fig. 7 is that the normalized saturation field H_s(ECC)/H_s(SL) calculated for $R = 7.5$ kOe/s over the range $0 \leqslant I \leqslant 3.0$ erg/cm2 exhibits a minimum value of H_s(ECC)/H_s(SL) = 0.81 (corresponding to H_s(ECC) = 8.7 kOe) at $I \approx 1.8$ erg/cm^2. This is not observed in Fig. 4 which only includes results for $0 \leqslant I \leqslant 1.8$ erg/cm^2. This indicates that the minimum value that is observed in the experimental data at $I \approx 1.2$ erg/cm^2 ($d \approx 1.0$ nm) in Fig. 4 with H_s(ECC) = 7.8 kOe, also appears in the simulations but at a somewhat higher value of I and H_s.

The second point to note is that while the value of H_s calculated for both dual and single layer media for $R = 10^7$ kOe/s is significantly larger than the corresponding results for $R = 7.5$ kOe/s, a comparison of the results presented in Fig. 7 show that the normalized values of H_s(ECC)/H_s(SL) track each other reasonably closely for smaller values of I. However, they start to diverge at $I \approx 1.8$ erg/cm^2 where the ratio H_s(ECC)/H_s(SL) calculated at the higher sweep rate drops below the corresponding ratio calculated for $R = 7.5$ kOe/s, which begins to increase for $I > 1.8$ erg/cm^2. Fig. 7 therefore suggests that the cap layer is more effective in reducing the switching field at higher sweep rates than the results from the lower sweep rate used in VSM measurements might indicate. In addition, not only is the minimum of the ratio H_s(ECC)/H_s(SL) lower for $R = 10^7$ kOe/s than for $R = 7.5$ kOe/s (0.75 vs 0.81), it occurs at a higher value of I (2.2 erg/cm^2 vs 1.8 erg/cm^2). This suggests that optimizing the spacer thickness to maximise the value of H_s at the higher sweep rates results in a larger gap (min[ΔE(ECC)/ΔE(SL)] $\approx$ 1.37 for $I = 2.2$ erg/cm^2) than if it is optimized it to maximize H_s at VSM sweep rates (min[ΔE(ECC)/ΔE(SL)] $\approx$ 1.28 for $I = 1.8$ erg/cm^2), thereby also increasing the stability of the bit pattern.

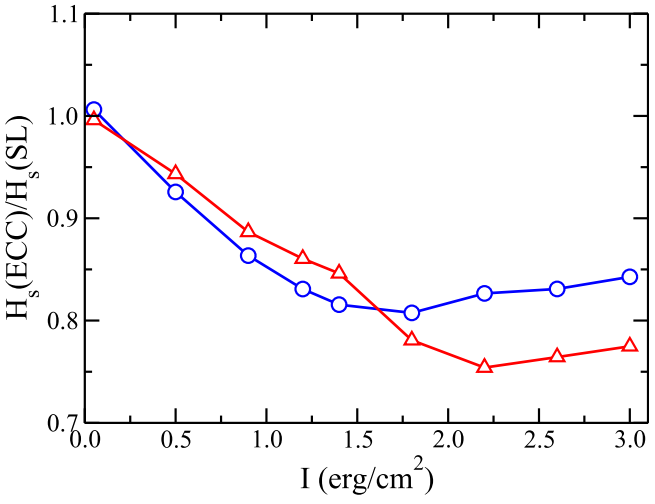

Fig. 7. Normalized saturation field H_s(ECC)/H_s(SL) obtained from simulations plotted as a function of the interlayer exchange constant I for $R = 7.5$ kOe/s (blue) and $R = 10^7$ kOe/s (red) over the range $0 < I < 3.0$ erg/cm^2. (For interpretation of the references to colour in this figure legend, the reader is referred to the web version of this article.)

5. Conclusions

A series of hybrid LLG/kMC simulation studies is applied to model MH loops and compared with experimental results on dual layer ECC media CoPtCrB/CoPtCrSiO in which the thickness of the spacer is varied. A set of material parameters for the granular oxide CoPtCrSiO, based on the values given in Ref. [20], are shown to give excellent agreement with the experimental MH loops on single layer media. The corresponding material parameters for the cap layer are determined so as to give a good fit to MH loops for the ECC data in the weak coupling limit $d = 3.0$ nm. These are assumed to be independent of the spacer thickness. The exchange coupling constant between the layers, which we denote by, I, is the only material parameter used in the simulation that depends on d and is chosen to best fit the experimental curves. An analysis of these results is shown in Fig. 3 which illustrates a nearly linear decrease in I with increasing d.

While the results obtained from these simulation studies give good overall agreement with the experimental MH loops for exchange coupled CoPtCrB/CoPtCrSiO media, there are nevertheless some quantitative difference between them. Most obvious is the dependence of the saturation field H_s on the spacer thickness. In particular, while both the experiments and the simulations yield a minimum value of H_s when plotted as a function of the value of the exchange coupling constant I, the location of the minima ($I = 1.2$ erg/cm^2 and 1.8 erg/cm^2 in the experimental and simulated MH loops, respectively) and the minimum value of H_s (7.8 kOe and 8.7 kOe in the experimental and simulated MH loops, respectively) do not quite agree. An examination of the MH loops presented in Fig. 2 indicates that this discrepancy may be attributed in part to the detailed nature of the tails of the MH loops as $M \rightarrow -1$. Such subtle differences in the simulated MH loops close to saturation did not became apparent until after the parameters had been determined, based on a single run, and the averaging over several runs completed. While a more systematic approach to fitting the simulated MH loops to those obtained experimentally would undoubtedly improve the agreement between them this would require a significant enhancement in computational efficiency of the kMC algorithm to be feasible. It may also be the case that the model employed in the analysis is too simplistic to capture the level of detail required to accurately determine the value of H_s. For example, the current model makes no provision, beyond the variation in the interlayer exchange, for the effect of the finite thickness and magnetic properties of the spacer layer.

That said, the results obtained nevertheless provide a good quantitative description of the experimental MH loops and capture all of their essential features. In addition, it is demonstrated how the methodology can be used to extend the results of MH loops obtained from VSM studies to calculate estimates of the other properties such as energy barriers and switching fields that are important in optimizing the performance of magnetic media, but

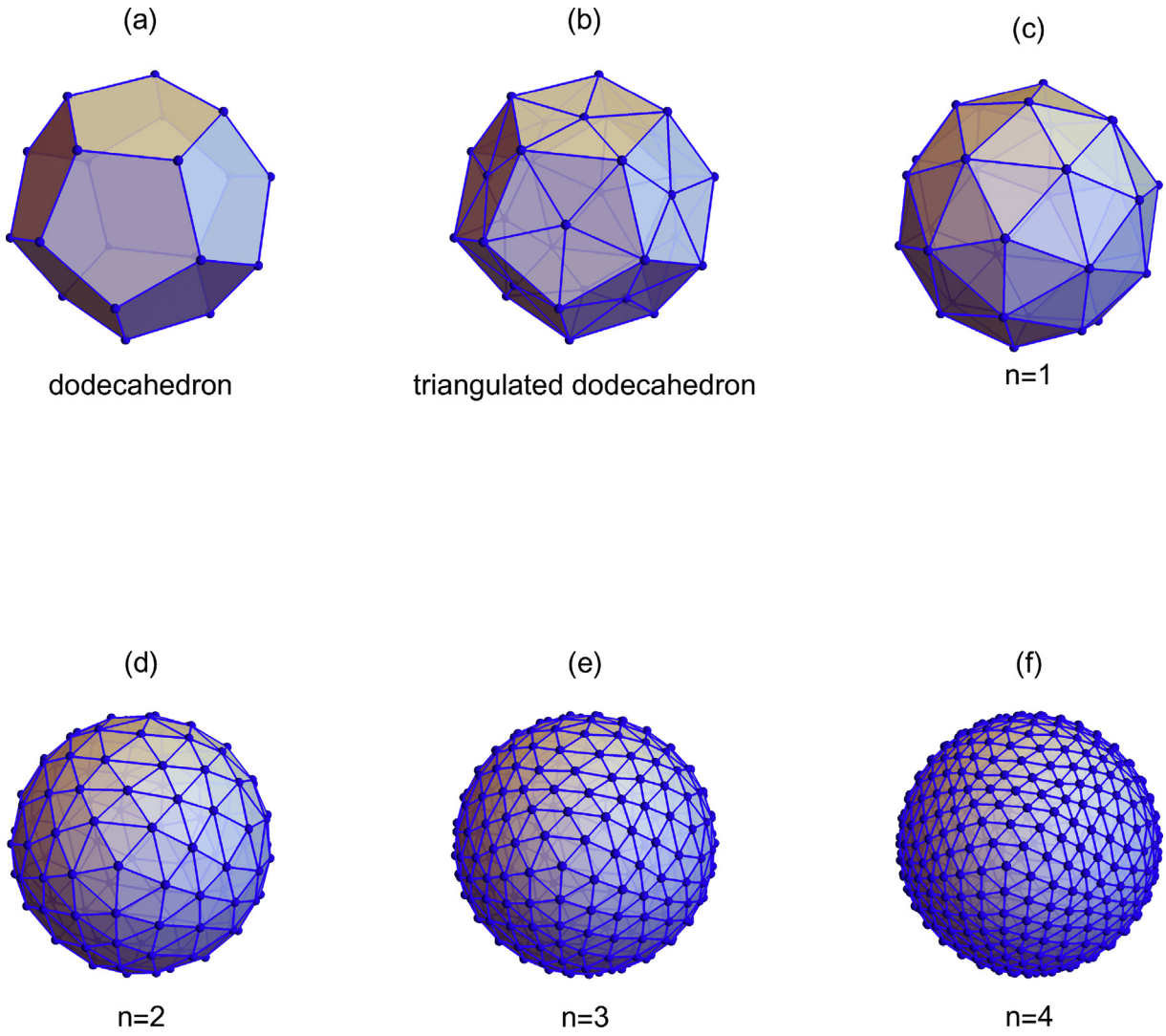

Fig. 8. The construction of the lattice used to discretize the points on the surface of the sphere begins with a dodecahedron shown in (a). The faces of the dodecahedron are then triangulated, as shown in (b) and the vertices of the triangulated dodecahedron projected onto the unit sphere, to generate the polyhedron shown in (c). This process can be iterated by successively triangulating the surfaces and projecting them out to the unit sphere. The triangulation was performed using the Mathematica "Geodesate" function. The polyhedra generated by successive degrees of subdivision labelled by the index n, with the triangulated dodecahedron shown in (c) assigned the index $n = 1$. Figures (d), (e) and (f) show the polyhedra $n = 2, 3$ and 4, respectively. Table 2 lists the number of vertices, edges and faces generated with each successive subdivision.

which are nevertheless difficult to access experimentally. This study demonstrates the significance of the kMC algorithm as one of the few methods that can be applied to simulate the collective behaviour of highly anisotropic magnetic materials that allows a quantitative comparison between experimental studies (in this case VSM measurements of MH loops) and simulations based on standard and well established micromagnetic models.

Acknowledgements

This work was supported by Western Digital Corporation, the Natural Science and Engineering Research Council (NSERC) of Canada, the Canada Foundation for Innovation (CFI), and the Atlantic Computational Excellence network (ACEnet).

Appendix A. Determination of the saddle points with discretized state space

The energy for a single grain in an effective field, given by Eq. (1), is expressed in terms of the orientation of the magnetic moment of each of the two layers comprising the grain. Since the orientation of each spin can be represented by a point on a unit sphere the state space for a system of two coupled Heisenberg grains is therefore given by the 4-dimensional manifold $S_A^2 \otimes S_B^2$ and the energy of the system, as expressed by Eq. (1), as a scalar function defined on this manifold. The problem is then to determine the location of the local energy minima and the saddle points connecting them on this manifold.

Given that the model does not assume that the direction of the effective fields or the uniaxial anisotropy of the two layers comprising the individual grains share common axes, symmetry arguments cannot be applied to reduce the dimensionality of the

Table 2
The number of vertices, edges and faces listed for the polyhedra for $1 \leqslant n \leqslant 4$ where the index n denotes the number of subdivisions of the orginal dodecahedron by triangulation.

Index	Vertices	Edges	Faces
$n = 1$	32	90	60
$n = 2$	122	360	240
$n = 3$	272	810	540
$n = 4$	482	1440	960

problem as in Ref. [18]. Also it cannot be assumed that, following the reversal of a given grain, the location and number of local minima and the saddle points connecting them can be inferred for all the other grains from their state prior to the reversal. This means that locating the local energy minima and the saddle points for each grain at each step in the kMC algorithm is a computationally complex task.

In this paper we have implemented a scheme whereby we discretize the state space by triangulating the surface of the spheres, S_A^2 and S_B^2, with a mesh representing a discrete set of states that are connected by a network of edges. This discretization and its construction, shown schematically in Fig. 8, begins by triangulating the faces of a dodecahedron as shown in Fig. 8(a) and (b). the vertices are then projected onto the unit sphere to form a polyhedron constructed from triangular faces shown in Fig. 8(c). This process can be iterated by triangulating the faces to form a polyhedra with an increasing finer mesh. Each successive triangulation is labelled by the index n with the original polyhedron shown in Fig. 8(c) assigned the index $n = 1$. The mesh used is the present calculation is based on one with $n = 2$ and is shown in Fig. 8(d).

Specifying the orientation of the magnetic moments of the A and B layers in terms of the position vectors $\alpha = (x_1, x_2)$ and $\beta = (y_1, y_2)$, where x_i and y_i denote some system of generalized coordinates that parameterize the unit sphere (e.g. spherical coordinates), the manifold $S_A^2 \otimes S_B^2$ can be parameterized in terms of the coordinates $(\alpha, \beta) = (x_1, x_2, y_1, y_2)$. Similarly, denoting the vertices on each of two polyhedron meshes representing the discretized state space of the A and B layers by the sets $V_A = \{v_a\}$ and $V_B = \{v_b\}$, with $a = \{1, 2 \ldots N_v\}$ and $b = \{1, 2 \ldots N_v\}$, respectively, the $S_A^2 \otimes S_B^2$ manifold can be discretized by the tensor product $V_A \otimes V_B = \{(v_a, v_b)\}$ where the point $(v_a, v_b) = (x_1(a), x_2(a), y_1(b), y_2(b))$. We will denote the vertex $(v_a, v_b) \equiv (a, b)$. Fig. 9 shows a schematic representation of two states (α, β) represented by the blue (α) and red (β) markers together with nearest discretized points, denoting the two states a and b, represented by the purple markers.

The discretized lattice can be used to determine the local minimum energy states by initializing the system at each of the points (a, b) and then relaxing the system to a local minimum by the method of steepest descent. Doing this for all pairs of vertices in

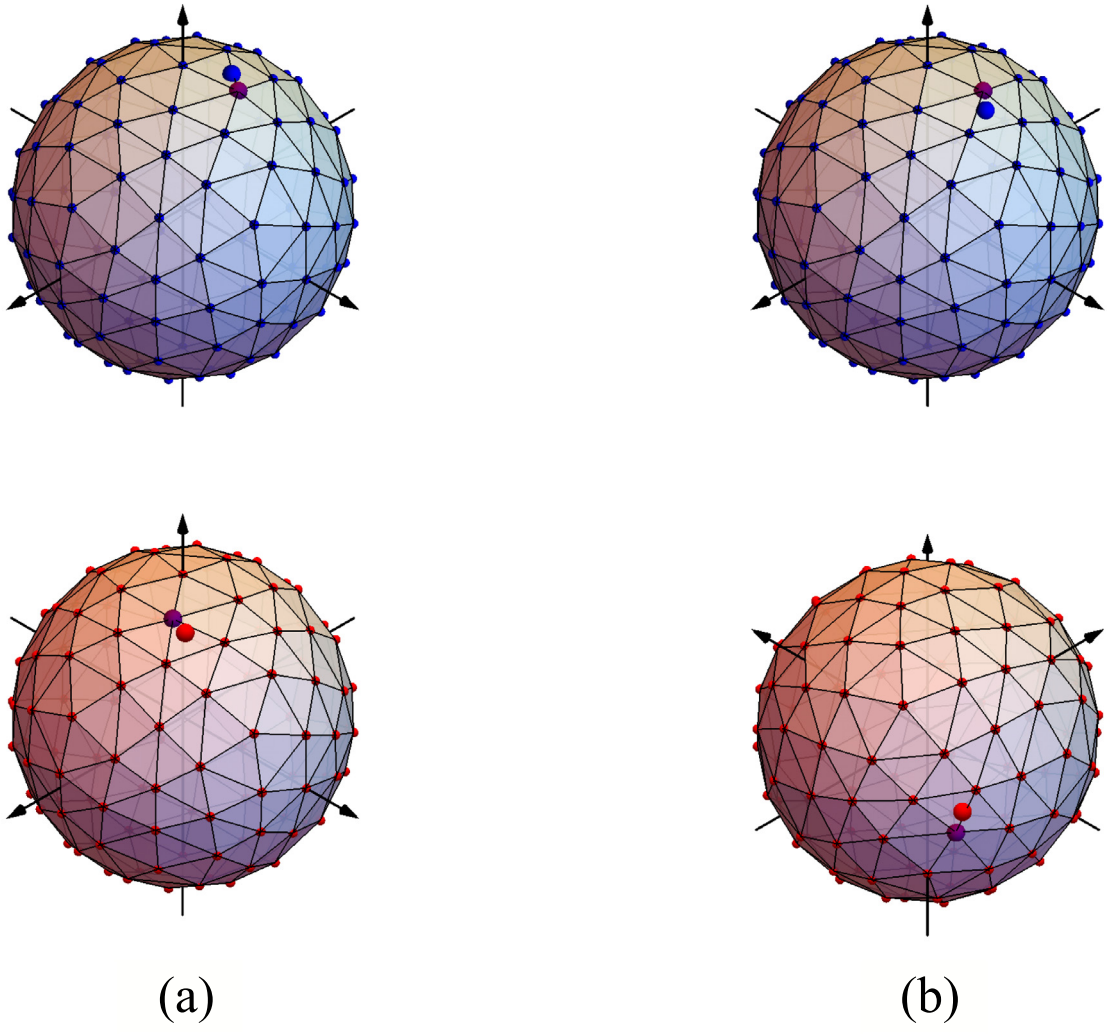

Fig. 9. The state space of the energy used to describe a single composite grain consisting of two exchange coupled moments may be represented by the manifold $S_A^2 \otimes S_B^2$ which defines the orientation of spin A and spin B, respectively. Two such states are denoted by blue and red points in (a) and (b). Figure (a) is an example of a ferromagnetically aligned grain in which both spins are orientated so the points α and β lie in the upper hemisphere while Fig. (b) is an example of an antiferromagnetically aligned grain in with the points α and β lie in the upper and lower hemispheres, respectively. Note that the coordinate axes in Fig. (b) have been rotated to better illustrate the vertices in the lower hemisphere.

parallel and clustering common states during the descents locate local energy minima. The location of these local minima, denoted by $\{\alpha,\beta\}$, will not in general correspond to a point represented by a pair of vertices (a,b) defined by the discrete lattice.

To obtain the saddle points connecting these minima is somewhat more complicated. The method we used in this work proceeds in two steps. We begin by considering pairs of local minima which we denoted by $(\alpha,\beta)_{\text{initial}}$ and $(\alpha,\beta)_{\text{final}}$ and identifying the vertices on the discretized lattice that lie closest to them, which we denote by $(a,b)_{\text{initial}}$ and $(a,b)_{\text{final}}$, respectively. This is shown schematically in Fig. 9 for two distinct states in which $(\alpha,\beta)_{\text{initial}}$ and $(\alpha,\beta)_{\text{final}}$ are represented by the blue and red markers, respectively and the closest $(a,b)_{\text{initial}}$ and $(a,b)_{\text{final}}$ discretized states by the purple markers.

In order to define a path connecting any two vertices requires specifying the edges that join pairs of vertices in $V_A \otimes V_B$. We consider two types of edges in $V_A \otimes V_B$ constructed from edges connecting the vertices $a \leftrightarrow a'$ in V_A, which we define as $e_{aa'}$, and those connecting the vertices $b \leftrightarrow b'$ in V_B, which we define as $e_{bb'}$. The first set we define as Nearest Neighbour Edges (NNEs) and are defined by $e_{aa'} \otimes \mathbb{I}_b$ and $\mathbb{I}_a \otimes e_{bb'}$, where $\mathbb{I}_a$ and $\mathbb{I}_b$ simply denote $a \leftrightarrow a$ and $b \leftrightarrow b$, respectively. These may be understood as follows. Consider the set of vertices a_k that share an edge with the vertex a as shown in Fig. 10(a), where the vertex a is denoted by the purple marker and the set $\{a_k\}$ denote the vertices that connect to the vertex a through the edges highlighted in purple. The NNE $e_{aa_k} \otimes \mathbb{I}_b$, therefore connects the vertex $\{a,b\} \leftrightarrow \{a_k,b\}$. Similarly we define the NNE $\mathbb{I}_a \otimes e_{bb_l}$ as connecting the vertex $(a,b) \leftrightarrow (a,b_l)$, where $\{b_l\}$ denotes the set of vertices in V_B that share a common edge with vertex b shown in Fig. 10(b), where the vertex b is denoted by the purple marker and the set $\{b_l\}$ the vertices that connect to the vertex b through the edges highlighted in purple. We also define the Next Nearest Edges $e_{aa_k} \otimes e_{bb_l}$ that connect the vertices $(a,b) \leftrightarrow (a_k,b_l)$.

The paths connecting the two vertices $(a,b)_{\text{initial}}$ and $(a,b)_{\text{final}}$ consist of a sequence of $L+1$ vertices, which we denote by $\{a_n,b_n\}$ with $1 \leqslant n \leqslant L+1$, connected by L edges with $(a_1,b_1) = (a,b)_{\text{initial}}$ and $(a_{L+1},b_{L+1}) = (a,b)_{\text{final}}$. We refer to L as the length of the path and, denoting the energy at the vertex (a,b) as $E(a,b)$, we define $E_{\max} = \max\{E(a_1,b_1),E(a_2,b_2)\ldots E(a_{L+1},b_{L+1})\}$, the maximum energy of the path. For the particular case in which $(a,b)_{\text{initial}}$ and $(a,b)_{\text{final}}$ denote the vertices that lie closest to the

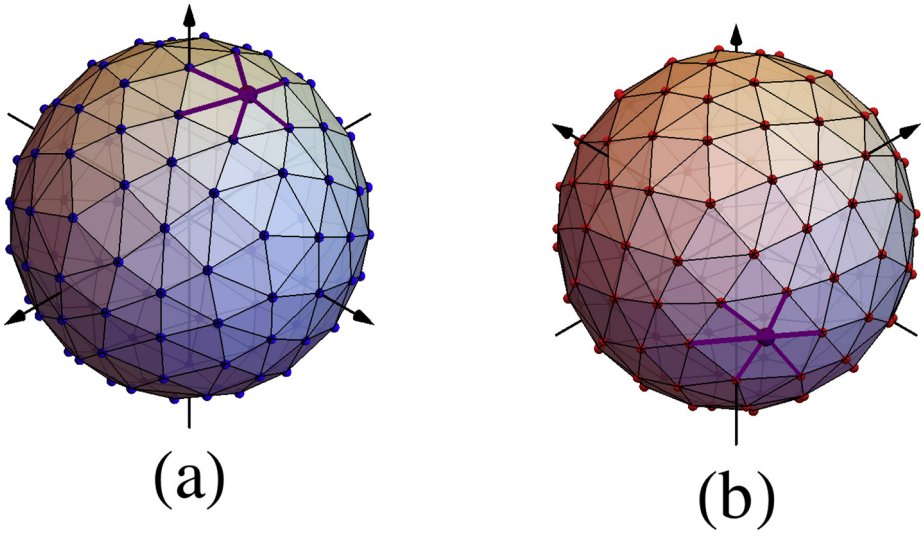

Fig. 10. Schematic showing (a) a vertex $v_a \in V_A$ (purple marker) together with all the edges that include v_a, denoted by e_{aa_k} (purple lines) and which connect to the vertices v_{a_k} and (b) a vertex $v_b \in V_B$ (purple marker) together with all the edges that include v_b, denoted by e_{bb_l} (purple lines) and which connect to the vertices v_{b_l}. (For interpretation of the references to colour in this figure legend, the reader is referred to the web version of this article.)

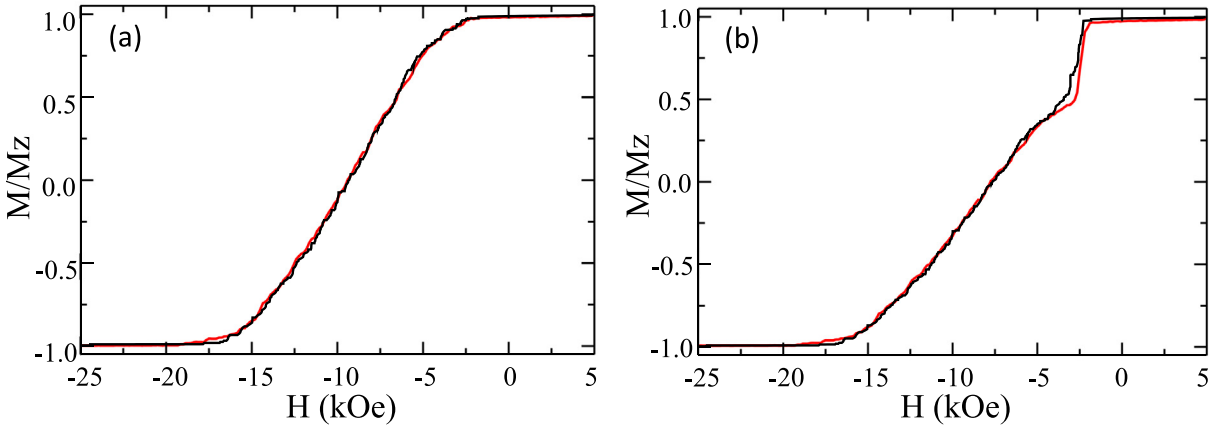

Fig. 11. Simulated MH loops for (a) single layer and (b) dual layer ECC CoPtCrB/CoPtCrSiO media with $I = 0.05$ erg/cm^2 calculated using finite temperature sLLG (red) and the hybrid LLG/kMC (black) algorithms for $R = 10^7$ kOe/s. While the data are for a single run only the nevertheless show remarkably good agreement, clearly demonstrating that the differences between the results for different R values presented in Figs. 6 and 7 are due to the different sweep rates not the algorithm used to calculate them.

local minimum energy states $(\alpha,\beta)_{\text{initial}}$ and $(\alpha,\beta)_{\text{final}}$ we define the optimal energy path connecting these two vertices as the path that minimizes (a) $E_{\max}$ and (b) L. The vertex with the maximum energy on the optimal energy path connecting the vertices $(a,b)_{\text{initial}}$ and $(a,b)_{\text{final}}$ provides an initial estimate of the location of the saddle point that connects the local energy minima $(\alpha,\beta)_{\text{initial}}$ and $(\alpha,\beta)_{\text{final}}$ that can be further refined by repeatedly fitting the energy surface to a quartic and solving for the saddle point algebraically.

While it is difficult to visualize paths on a four dimensional mesh it is, in this case at least, straightforward to construct and enumerate all distinct paths connecting any two vertices. Using the Bellman-Ford [22] algorithm it is possible to efficiently search every path connecting any pair of local minima and determine the optimal energy path.

Appendix B. Comparison of kMC and sLLG algorithms

MH hysteresis loops for $R = 10^7$kOe/s obtained using both sLLG and the hybrid LLG/kMC formalism are presented in Fig. 11 for both single layer and dual layer media with $I = 0.05$ erg/cm^2. Both sets of data are from a single run and while there are minor quantitative differences the agreement between the two data sets is quite remarkable.

This is consistent with earlier results in which MH loops calculated over a range of sweep rates using both sLLG and the hybrid LLG/kMC method are compared [17,18] and are shown to be in good agreement. The range of sweep rates over which this agreement extends is limited by the computational time required to generate an MH loop using sLLG at very low sweep rates and by the increasing importance of dynamical effects in the reversal process at very high sweep rates. However, for the sweep rates considered in this study the dependence of the magnetization on the applied field is dominated by thermally activated reversal of the magnetization within the individual grains. Therefore, while in principle at least, the field dependence of the magnetization can be modelled equally well using either sLLG or the hybrid LLG/kMC method, at sweep rates used in the experimental VSM studies, the computational times required by sLLG are such that it is not a feasible approach.

References

[1] M. Plumer, J. van Ek, D. Weller, (Eds.), The Physics of Ultra-High-Density Magnetic Recording, Springer, Berlin, 2001. M.L. Plumer, J. van Ek, W. Cain, Phys. Canada 67 (2011) 25.
[2] H.J. Richter, A. Lyberatos, U. Nowak, R.F.L. Evans, R.W. Chantrell, J. Appl. Phys. 111 (2012) 033909.
[3] R.H. Victora, X. Shen, IEEE Trans. Magn. 41 (2005) 537.
[4] J.-P. Wang, W. Shen, S.-Y. Hong, IEEE Trans. Magn. 43 (2007) 682.
[5] D. Suess, J. Lee, J. Fidler, T. Schrefl, J. Magn. Magn. Mater. 321 (2009) 545.
[6] M.L. Plumer, M.C. Rogers, E. Meloche, IEEE Trans. Magn. 45 (2009) 3942.
[7] W. Brown Jr., Phys. Rev. 130 (1963) 1677.
[8] R.W. Chantrell, A. Lyberatos, E.P. Wohlfarth, J. Phys. F: Met. Phys. 16 (1986) L145.
[9] Y. Kanai, S.H. Charap, IEEE Trans. Magn. 27 (1991) 4972.
[10] P.-L. Lu, S.H. Charap, J. Appl. Phys. 75 (1994) 5768.
[11] S.H. Charap, P.-L. Lu, Y. He, IEEE Trans. Magn. 33 (1997) 978.
[12] O. Hovorka, R.F.L. Evans, R.W. Chantrell, A. Berger, Appl. Phys. Lett. 97 (2010) 062504.
[13] G.J. Parker, W.N.G. Hitchon, Phys. Lett. A 377 (2013) 2388.
[14] G.D. Chaves-O'Flynn, G. Wolf, J.Z. Sun, A.D. Kent, Phys. Rev. Appl. 4 (2015) 024010.
[15] R.P. Tan, J. Carrey, M. Respaud, Phys. Rev. B 90 (2014) 214421.
[16] P. Chureemart, J. Chureemart, R.W. Chantrell, J. Appl. Phys. 119 (2016) 063903.
[17] T.J. Fal, J.I. Mercer, M.D. Leblanc, J.P. Whitehead, M.L. Plumer, J. van Ek, Phys. Rev. B 87 (2013) 064405.
[18] A.M. Almudallal, J.I. Mercer, J.P. Whitehead, M.L. Plumer, J. van Ek, T.J. Fal, Phys. Rev. B 92 (2015) 134418.
[19] T.J. Fal, M.L. Plumer, J.I. Mercer, J.P. Whitehead, J. van Ek, K. Srinivasan, Appl. Phys. Lett. 102 (2013) 202404.
[20] G. Choe, Y. Ikeda, K. Zhang, K. Tang, M. Mirzamaani, IEEE Trans. Magn. 45 (2009) 2694.
[21] R. Wood, IEEE Trans. Magn. 45 (2009) 100.
[22] R. Bellman, Q. Appl. Math. 16 (1958) 87; L.R. Ford, Network Flow Theory, Santa Monica, CA, RAND Corporation, 1956; E.F. Moore, Proc. International Symposium on Switching Theory 1957, Part II Harvard Univ. Press, Cambridge, Mass., 1959.
[23] A.F. Voter, in: K.E. Sickafus, E.A. Kotomin, B.P. Uberuaga (Eds.), Radiation Effects in Solids, Springer, Berlin, 2007.
[24] J.I. Mercer, MagLua is in-house stochastic micromagnetic simulation software with Lua scripting interface. < https://github.com/jasonimercer/maglua>.